J. Fluid Mech. (2009), *vol.* 637, *pp.* 213–239.
doi:10.1017/S002211200999053X

On the asymptotic behaviour of large-scale turbulence in homogeneous shear flow

JUAN C. ISAZA[1,2] AND LANCE R. COLLINS[1]†

[1]Sibley School of Mechanical & Aerospace Engineering, Cornell University, Ithaca, NY 14853–7501, USA

[2]Department of Mechanical Engineering, EAFIT University, Medellin, Colombia

(Received 12 January 2009; revised 15 May 2009; accepted 18 May 2009; first published online 17 September 2009)

The asymptotic behaviour of large-scale velocity statistics in an homogeneous turbulent shear flow is investigated using direct numerical simulations (DNS) of the incompressible Navier–Stokes equations on a 512^3 grid, and with viscous rapid distortion theory (RDT). We use a novel pseudo-spectral algorithm that allows us to set the initial value of the shear parameter in the range 3–30 without the shortcomings of previous numerical approaches. We find there is an explicit dependence of the early-time behaviour on the initial value of the shear parameter. Moreover, the long-time asymptotes of large-scale quantities such as the ratio of the turbulent kinetic energy production rate over dissipation rate, the Reynolds stress anisotropic tensor and the shear parameter itself depend *sensitively* on the initial value of the shear parameter over the range of Reynolds number we could achieve ($26 \leqslant R_\lambda \leqslant 63$) with the stringent resolution requirements that were satisfied. To gain further insight into the matter, we analyse the full *viscous* RDT. While inviscid RDT has received a great deal of attention, viscous RDT has not been fully analysed. Our motivation for considering viscous RDT is so that the energy dissipation rate enters the problem, enabling the shear parameter to be defined. We show asymptotic expansions for the short-time behaviour and numerically evaluate the integrals to determine the long-time prediction of viscous RDT. The results are in quantitative agreement with DNS for short times; however, at long times viscous RDT predicts the turbulent energy decays to zero. Through an analysis of the pressure–strain terms, we show that the nonlinear 'slow' terms are essential for rearranging turbulent energy from the streamwise direction to the mean shear direction, and this sustains the indefinite growth of the kinetic energy at long times. In effect, the nonlinear pressure–strain correlation maintains the three-dimensionality of the turbulence, countering the tendency of the mean shear to project the turbulence onto the two-dimensional plane of the mean-flow streamlines. We postulate that the predictions of viscous RDT at long times could be improved by introducing a model for the 'slow' pressure–strain term, along the lines of the Rotta model.

1. Introduction

Homogeneous turbulent shear flow (HTSF) is among the canonical flows considered to be the 'building blocks' of turbulence. It is the next step up in complexity from isotropic turbulence. This flow has many of the features found in wall-bounded flows,

† Email address for correspondence: lc246@cornell.edu

e.g. off-diagonal Reynolds stress components, turbulence production and hairpin vortices, without introducing the complexities of a fully inhomogenous turbulence. Consequently, this flow has been widely investigated in experiments, direct numerical simulations (DNS) and theoretically. Despite the attention it has received over the past 40+ years, there remain fundamental questions about the long-time behaviour of the flow that have yet to be satisfactorily resolved. In this study, we consider these issues using DNS and by applying rapid distortion theory (RDT).

In the classical view of HTSF (Tavoularis 1985; see also § 5.4.5 in Pope 2000 for a simple derivation), the turbulent kinetic energy at long times grows according to

$$q^2(t) = q_r^2 \exp(\sigma S t), \tag{1.1}$$

where $q^2 \equiv \overline{u_i' u_i'}$ is twice the turbulent kinetic energy, S is the uniform mean shear rate, σ is a yet-undefined constant and the subscript '$_r$' indicates a reference value. Much of the literature supports $\sigma > 0$, although, as noted below, this is not universal. As noted by Jacobitz, Sarkar & van Atta (1997) for stratified turbulence and Schumacher, Sreenivasan & Yeung (2003) in their study of the small scales, two initial parameters characterize HTSF: the Reynolds number (here we use the Reynolds number based on the Taylor microscale, $R_\lambda \equiv q^2\sqrt{5/(3\epsilon\nu)}$, where ϵ is the dissipation rate and ν is the kinematic viscosity of the fluid); and the non-dimensional 'shear parameter' defined as $S^* \equiv Sq^2/\epsilon$. The latter is a measure of the strength of the shear relative to the turbulence time scale—$S^* \gg 1$ implies strong shear (note that $S^* \sim 30$ in a boundary layer). Technically, asymptotically strong shear would imply the more stringent condition: $S\tau_\eta \gg 1$, where $\tau_\eta \equiv (\nu/\epsilon)^{1/2}$ is the Kolmogorov time scale, or equivalently $S^* \gg R_\lambda$. This condition is rarely satisfied in DNS or experiments due to different, but important intrinsic limitations to both approaches.

Experimental measurements of a nearly HTSF are often made in a wind tunnel or water tunnel by passing turbulence through a screen with variable solidity that produces a nearly uniform mean velocity gradient across the tunnel. The resulting turbulence is not perfectly homogeneous, as the turbulence across any cross-section of the tunnel will have evolved for a period of time that too varies across the tunnel with the mean velocity. Hence there will be some turbulent transfer of kinetic energy in the direction of the mean gradient. The assumption made in most experiments is that this spatial diffusion of turbulent energy is small as compared to the source and sink terms. This assumption can be justified by computing the turbulent flux. Indeed, the turbulent flux is one or more orders of magnitude below the source and sink terms (Harris, Graham & Corrsin 1977).

Whether the asymptotic state of HTSF is a function of the initial value of either or both parameters remains controversial. Experiments have generally yielded $\sigma > 0$ (e.g. Harris *et al.* 1977; Tavoularis & Corrsin 1981; Rohr *et al.* 1988; Tavoularis & Karnik 1989; DeSouza, Nguyen & Tavoularis 1995), although with values that vary with the flow parameters (e.g. Garg & Warhaft 1998) and possibly the apparatus (Rose 1966, 1970; Champagne, Harris & Corrsin 1970). Tavoularis (1985) attempted to explain these discrepancies based on the initial value of the mean shear with some success.

Rohr *et al.* (1988) measured turbulence intensities in a water tunnel designed to allow them to vary the mean shear while keeping the centreline velocity of the tunnel constant. They found that the turbulence intensities grew faster for the higher shear rates at the same centreline speed. They also were able to vary the initial integral length scale of the turbulence and found that this too influenced the growth rate of the turbulence intensity (i.e. σ). Notice that both of these results are an indirect indication

of sensitivity to the shear parameter since it could have been defined in terms of the integral length scale as follows: $S^* = SL_{11}/q$, where L_{11} is the integral length scale. Similar results were obtained by Rose (1970), although subsequent concerns have been raised about the relatively short test section ($St \leqslant 3$). So while trends indicate some sensitivity to the shear parameter, it is clear that a comprehensive understanding of how σ depends upon the two initial parameters has yet to be developed.

There are two important challenges to the experiments that, to some extent, have limited their ability to address this question. First, the maximum value of St that can be achieved is limited by the length of the wind tunnel to $\leqslant 20$ for most experiments. It is difficult to tell if the asymptotic regime has been fully achieved. Some argue that it depends on the number of large eddy turnover times that have transpired, which is even more limited by the length of the tunnel. Second, while it is possible to explore a broad range of Reynolds numbers using an active grid (Mydlarski & Warhaft 1996), it is difficult in the wind tunnel to vary the shear parameter over a wide range. With the exception of DeSouza *et al.* (1995), the experiments are generally limited to $S^* \leqslant 10$, which while greater than unity, cannot be considered asymptotically large.

DNS of HTSF likewise have yielded mixed results. For example, Jacobitz *et al.* (1997) and Jacobitz & Sarkar (1999) in DNS studies of uniformly sheared stratified flows (at their lowest Richardson number) found that the asymptotic state of the flow depended sensitively on both the Reynolds number and the shear parameter. At low values of S_0^* the turbulence grew (i.e. $\sigma > 0$), but at larger values of S_0^* the turbulence decayed for all the initial values of Reynolds number they investigated. Shih *et al.* (2000) found a similar result, but argued that the sensitivity to S_0^* vanishes at large enough values of the Reynolds number ($R_\lambda \geqslant 80$). Lee, Kim & Moin (1990) did not consider this question directly, but in figure 4 of their paper they showed the asymptote for S^* to be sensitive to its initial value, S_0^*.

There have been numerical studies of flows closely related to HTSF as well. Yu & Girimaji (2005) applied a lattice Boltzmann algorithm to turbulent Couette flow and considered the early-time solution far from the boundaries to be similar to HTSF. They observed exponential growth of the kinetic energy and found only a weak sensitivity of the flow to S_0^* and a much stronger sensitivity to the initial value of R_λ. Schumacher (2004) studied turbulent flow confined between two free-slip planes subject to a body force that varies linearly from the top plane to the bottom. The resulting flow achieved a steady state at long times, implying $\sigma = 0$. Of course, there is likely significant influence of the bounding planes on the long-time behaviour of the turbulence, and hence this particular result may be an artifact of the flow specification.

Figure 1 shows a compilation of the S^*–R_λ parameter space that has been explored by DNS (solid symbols) and experiments (open symbols) in the literature, with the newest runs from this study designated by $\otimes$. For DNS, the standard definitions of S^* and R_λ apply, whereas for the experiments, various surrogates have been employed. For example, ϵ has been obtained as the imbalance of the turbulent kinetic energy production and growth (Harris *et al.* 1977; Tavoularis & Corrsin 1981; Tavoularis & Karnik 1989; DeSouza *et al.* 1995), or based on some combination of velocity derivatives (Rohr *et al.* 1988; Garg & Warhaft 1998; Shen & Warhaft 2000). The Taylor microscale was often estimated using one component of velocity, $\lambda = \overline{u^2}/\overline{(\partial u/\partial x)^2}$. An exception is DeSouza *et al.* (1995), who used the following empirical estimate: $\lambda^2 = 12\nu q^2/\epsilon$. In some cases (Garg & Warhaft 1998; Shen & Warhaft 2000), the definition of S^* reported in the paper differed from our definition. To compare with the other experiments, we recalculated those quantities using the

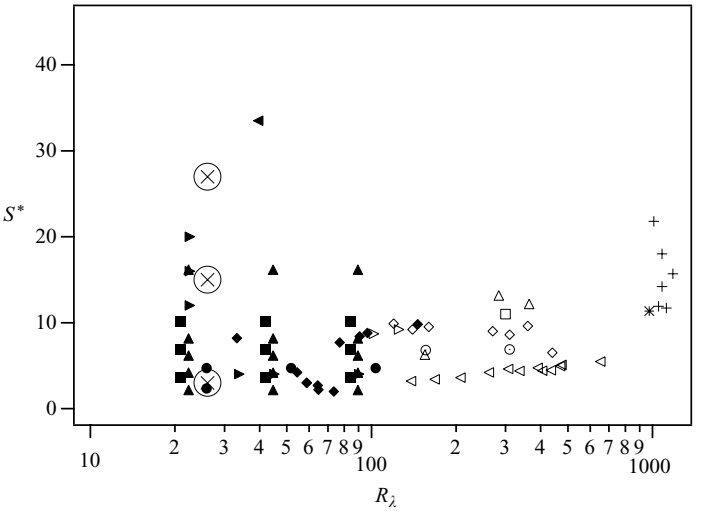

FIGURE 1. Initial values of the Reynolds number and the shear parameter for previous DNS (solid symbols) and operational values for previous experiments (open symbols) of HTSF. DNS: ● Rogers, Moin & Reynolds (1986), ◄ Lee *et al.* (1990), ► Jacobitz *et al.* (1997), ▲ Shih *et al.* (2000), ◆ Schumacher (2004) and ■ Yu & Girimaji (2005). Experiments: ○ Champagne *et al.* (1970), △ Tavoularis & Corrsin (1981), □ Harris *et al.* (1977), ◇ Tavoularis & Karnik (1989), + DeSouza *et al.* (1995), ⊙ Garg & Warhaft (1998), * Shen & Warhaft (2000), ◁ Ferchichi & Tavoularis (2000) and ▷ Rohr *et al.* (1988). The new runs from this study are designated by ⊗.

approximation $q^2 = \overline{u^2} + 2\overline{v^2}$. However, this correction could not be applied to the data of Ferchichi & Tavoularis (2000), as they only reported one component of the velocity; instead we assumed $q^2 = 2\overline{u^2}$.

Despite these unavoidable inconsistencies in the parameter definitions, figure 1 shows reasonably well the regions of the parameter space that have been explored by simulations and experiments. In particular, it is apparent that DNS has had difficulty exploring both high Reynolds number and high shear parameter. Most DNS are based on the algorithm by Rogallo (1981), which requires remeshing at odd integer values of St (i.e. $St = 1$, 3, 5, etc.). Remeshing, combined with dealiasing leads to a sudden loss in both the turbulent kinetic energy and turbulent energy dissipation rate. For higher shear rates, this loss can be as large as 20 %–40 %. Lee *et al.* (1990) reached $S_0^* \sim 30$ using the Rogallo code by turning off the remeshing step. They argued that at high shear rates, the adverse effect of the frequent remeshing exceeds the benefits, particularly in light of the relatively short physical time of the simulation. In contrast, experiments are able to span a much broader range of Reynolds numbers, but they too are limited to a modest range of the shear parameter.

The shortcomings of the Rogallo algorithm at high S_0^* have been addressed by a new algorithm (Brucker *et al.* 2007). Their approach too is based on a pseudo-spectral algorithm for the Navier–Stokes equations; however, the field variables in physical space are evaluated on an orthogonal mesh in the laboratory frame instead of the deforming mesh used by the Rogallo algorithm. The resulting DNS has smaller aliasing errors, and no jumps in the kinetic energy or dissipation rate, since the remeshing step has been eliminated. In this investigation, we apply the new algorithm to a series of 512^3 DNS of shear flows with initial shear parameters over the range 3–30. Owing to the stringent resolution requirements enforced in this study (see § 3.3

for details), the range of Reynolds numbers was relatively small ($26 \leqslant R_\lambda \leqslant 63$); however, the results were found to depend only weakly on this parameter. We present new findings for the asymptotic behaviour of the large-scale quantities, as well as attempt to sort out the inconsistencies in the previous literature.

Additionally, to assist in the interpretation of the high shear results, we apply RDT to HTSF. Scaling arguments suggest that for cases in which the shear parameter is high, the nonlinear turbulence–turbulence interactions can be neglected from the equation of motion. A review of the theory can be found in Savill (1987) and Hunt & Carruthers (1990). RDT has been applied to *inviscid* HTSF by Moffat (1967), Townsend (1970), and more recently by Rogers (1991), who developed analytical expressions for the short- and long-time behaviour of the Reynolds stress components. However, the Reynolds number and shear parameter are not defined in the inviscid limit, and hence this RDT analysis cannot be used to investigate the significance of these parameters on the long-time behaviour of the turbulence. RDT has also been applied to *viscous* HTSF (Deissler 1961; Fox 1964; Thacker, Grosh & Gatski 1999); however, their results do not consider the significance of the shear parameter on the turbulence evolution.

In this study, we obtain analytical expressions for the short-time behaviour of the turbulent Reynolds stresses, kinetic energy production over dissipation rate and the shear parameter. The results explicitly show how the two parameters influence the short-term behaviour. Second, we numerically evaluate the viscous RDT integrals to obtain predictions for the asymptotic behaviour of HTSF at long times. Comparing viscous RDT to DNS helps explain why nonlinear effects eventually become important, and suggests possible modifications to the theory that could account for these effects.

The paper is organized as follows. Section 2 discusses the governing equations for HTSF, with the equations for the large-scale turbulence statistics provided in § 2.4. Results from the DNS are presented in § 3 followed by the viscous RDT analysis in § 4. Conclusions are given in § 5.

2. Homogeneous turbulent shear flow

2.1. *Governing equations*

We are interested in the flow of an incompressible fluid in a periodic box of length 2π in each direction. The governing equations for the fluid are

$$\frac{\partial u_i}{\partial x_i} = 0, \tag{2.1}$$

$$\frac{\partial u_i}{\partial t} + u_j \frac{\partial u_i}{\partial x_j} = -\frac{\partial (p/\rho)}{\partial x_i} + \nu \frac{\partial^2 u_i}{\partial x_j \partial x_j}, \tag{2.2}$$

where u_i is the velocity vector, ρ is the fluid density, ν is the kinematic viscosity and p is the pressure.

Introducing the Reynolds decomposition, $u_i = U_i + u_i'$ and $p = P + p'$, where capital letters represent mean quantities and prime letters are the fluctuating quantities. We define $U_i = (Sx_2, 0, 0)$, where S is the spatially uniform mean shear rate imposed on the flow. Invoking homogeneity and combining and simplifying the terms that involve

the mean flow, the final form of the evolution equation for the fluctuating velocity is

$$\frac{\partial u_i'}{\partial t} + \underbrace{Sx_2\frac{\partial u_i'}{\partial x_1} + S\delta_{i1}u_2'}_{\text{rapid}} + \underbrace{u_j'\frac{\partial u_i'}{\partial x_j}}_{\text{slow}} = -\frac{\partial(p'/\rho)}{\partial x_i} + \nu\frac{\partial^2 u_i'}{\partial x_j \partial x_j}. \tag{2.3}$$

The terms that are proportional to the mean shear rate S are labelled 'rapid' and the nonlinear terms are labelled 'slow'. Taking the divergence of (2.3) while invoking the continuity relationship shown in (2.1) yields the following Poisson equation for the pressure

$$\frac{1}{\rho}\frac{\partial^2 p'}{\partial x_i \partial x_i} = \underbrace{-2S\frac{\partial u_2'}{\partial x_1}}_{\text{rapid}} \underbrace{-2\frac{\partial u_i'}{\partial x_j}\frac{\partial u_j'}{\partial x_i}}_{\text{slow}}. \tag{2.4}$$

2.2. *Initial conditions*

The initially isotropic velocity field was generated using a random phase algorithm with a prescribed initial energy spectrum $E_0(k_0)$ given by

$$E_0(k_0) = C_\kappa \epsilon_0^{2/3}\kappa_0^{-5/3}\begin{cases}(k_0/\kappa_0)^2 & k_0 < \kappa_0\\ (k_0/\kappa_0)^{-5/3} & \kappa_0 \leqslant k_0 \leqslant \kappa_\eta\\ 0 & k_0 > \kappa_\eta\end{cases}, \tag{2.5}$$

where k_0 is the initial wavenumber, $C_\kappa \approx 1.5$ is the Kolmogorov constant, ϵ_0 is the initial energy dissipation rate, κ_0 defines the location of the peak in the energy spectrum and κ_η is the maximum energy-containing wavenumber, defined to be consistent with ϵ_0 as

$$\frac{\kappa_\eta}{\kappa_0} \equiv \left[\frac{2\epsilon_0^{1/3}}{3\nu C_\kappa \kappa_0^{4/3}} + \frac{11}{15}\right]^{3/4}. \tag{2.6}$$

The spectrum includes an energy containing range proportional to k_0^2 in order to minimize the time required for the simulation to reach the self-similar state.

To check whether the results depend upon the Gaussian velocity field that results from the random-phase initialization, we compared them to separate runs that first let the turbulence decay without mean shear until the velocity derivative skewness, $M_3 \equiv \overline{(\partial u/\partial x)^3}/\left[\overline{(\partial u/\partial x)^2}\right]^{3/2}$, had reached the fully developed value of -0.4 (Tavoularis & Corrsin 1981), so that the small scales were in a more natural state before applying the uniform shear. The comparison is shown in figure 2. As you can see, the large scales are not significantly affected by this change in the initial velocity field, and hence the Gaussian initial velocity field was used throughout this study.

2.3. *Parameters*

HTSF is characterized by two initial parameters: the Reynolds number defined as $R_\lambda \equiv q^2\sqrt{5/(3\nu\epsilon)}$ and the shear parameter defined as $S^* \equiv Sq^2/\epsilon$. The first is a measure of the ratio of the largest to the smallest turbulence length or time scales, while the second is the ratio of the largest turbulence time scale to the mean shear time scale, taken as $1/S$. It is customary to define a non-dimensional time $\beta \equiv St$, which corresponds to the total strain due to the mean shear.

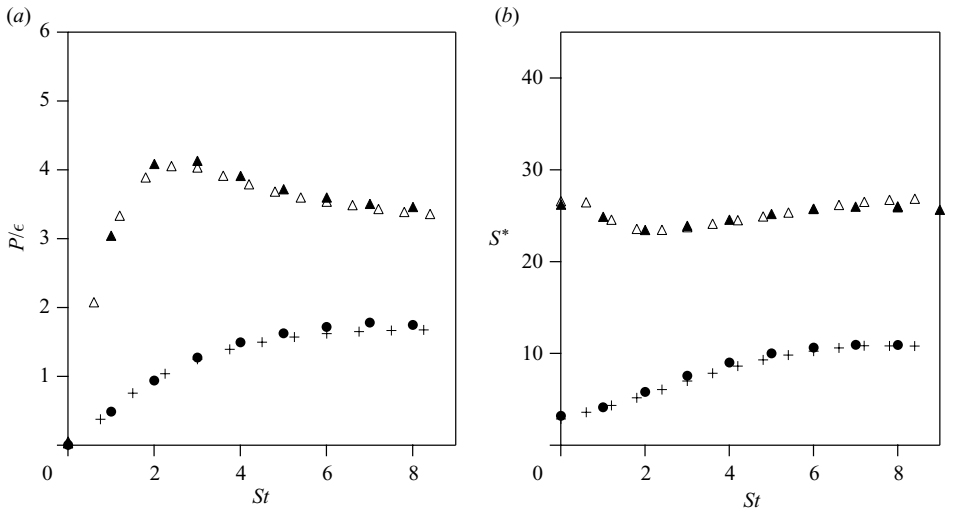

FIGURE 2. Temporal evolution of (*a*) P/ϵ and (*b*) S^* for Gaussian turbulence with $S_0^* = 3$ + and 27 △, and for an isotropic field in which the turbulence has decayed until the velocity derivative skewness, $M_3 \equiv \overline{(\partial u/\partial x)^3}/\left[\overline{(\partial u/\partial x)^2}\right]^{3/2}$, has reached the fully developed value of −0.4 with $S_0^* = 3$ ● and 27 ▲. The initial Reynolds number is $(R_\lambda)_0 = 26$.

2.4. *Reynolds averaged equations*

The exact equations governing the four non-zero components of the average Reynolds stress are (Pope 2000)

$$\frac{\mathrm{d}R_{11}}{\mathrm{d}t} = P_{11} + \Pi_{11} - \epsilon_{11}, \tag{2.7a}$$

$$\frac{\mathrm{d}R_{22}}{\mathrm{d}t} = \quad + \Pi_{22} - \epsilon_{22}, \tag{2.7b}$$

$$\frac{\mathrm{d}R_{33}}{\mathrm{d}t} = \quad + \Pi_{33} - \epsilon_{33}, \tag{2.7c}$$

$$\frac{\mathrm{d}R_{12}}{\mathrm{d}t} = P_{12} + \Pi_{12} - \epsilon_{12}, \tag{2.7d}$$

where

$$R_{ij} \equiv \overline{u_i' u_j'}, \tag{2.8}$$

$$P_{ij} \equiv -R_{ik}\frac{\partial \overline{u}_j}{\partial x_k} - R_{jk}\frac{\partial \overline{u}_i}{\partial x_k}, \tag{2.9}$$

$$\Pi_{ij} \equiv \overline{\frac{p'}{\rho}\left(\frac{\partial u_i'}{\partial x_j} + \frac{\partial u_j'}{\partial x_i}\right)}, \tag{2.10}$$

$$\epsilon_{ij} \equiv 2\nu\overline{\frac{\partial u_i'}{\partial x_k}\frac{\partial u_j'}{\partial x_k}}. \tag{2.11}$$

The source terms for HTSF take the form: $P_{11} = -2SR_{12}$ and $P_{12} = -SR_{22}$. Taking half of the trace of (2.7) yields the transport equation for the turbulent kinetic energy

$$\frac{\mathrm{d}q^2/2}{\mathrm{d}t} = P - \epsilon, \tag{2.12}$$

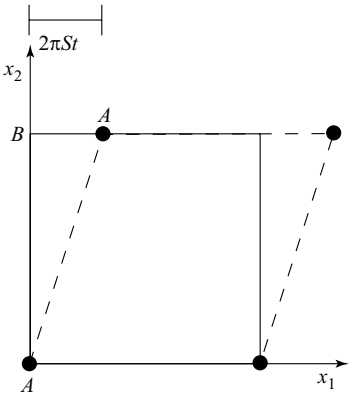

FIGURE 3. Schematic of the shear periodic boundary conditions in two dimensions. Mean shear of magnitude S lies in the vertical direction. Solid lines indicate orthogonal frame; dashed lines indicate deforming frame in which boundary conditions are periodic. Black dots are periodic points.

where $P \equiv P_{11}/2$ and $\epsilon \equiv \epsilon_{ii}/2$. To analyse the self-similar regime of HTSF, it is useful to consider the anisotropic Reynolds stress tensor, $b_{ij} \equiv R_{ij}/q^2 - \delta_{ij}/3$. We expect this tensor to approach a constant in the self-similar regime. The exact governing equations for the four non-zero components of the anisotropic tensor are as follows:

$$\frac{1}{S}\frac{\mathrm{d}b_{11}}{\mathrm{d}t} = 2\left(b_{11}+1/3\right)\left(b_{12}+1/S^*\right) - 2b_{12} + \tilde{\Pi}_{11} - \tilde{\epsilon}_{11}, \tag{2.13a}$$

$$\frac{1}{S}\frac{\mathrm{d}b_{22}}{\mathrm{d}t} = 2\left(b_{22}+1/3\right)\left(b_{12}+1/S^*\right) + \tilde{\Pi}_{22} - \tilde{\epsilon}_{22}, \tag{2.13b}$$

$$\frac{1}{S}\frac{\mathrm{d}b_{33}}{\mathrm{d}t} = 2\left(b_{33}+1/3\right)\left(b_{12}+1/S^*\right) + \tilde{\Pi}_{33} - \tilde{\epsilon}_{33}, \tag{2.13c}$$

$$\frac{1}{S}\frac{\mathrm{d}b_{12}}{\mathrm{d}t} = 2b_{12}\left(b_{12}+1/S^*\right) - \left(b_{22}+1/3\right) + \tilde{\Pi}_{12} - \tilde{\epsilon}_{12}, \tag{2.13d}$$

where $\tilde{\Pi}_{ij} \equiv \Pi_{ij}/Sq^2$ and $\tilde{\epsilon}_{ij} \equiv \epsilon_{ij}/Sq^2$.

3. Direct numerical simulations

3.1. *Numerical method*

The DNS code integrates the continuity relationship (2.1) and the equation for the fluctuating velocity (2.3). The boundary condition in the x_2 direction is not periodic in the laboratory frame of reference due to the presence of the uniform shear. Figure 3 shows a schematic of the boundary condition in two dimensions. The dashed lines show the deforming frame of reference in which the flow is periodic. The solid lines indicate the orthogonal laboratory frame of reference. Forward and reverse spectral transforms for a generic variable ζ, expressed in terms of the orthogonal frame of reference, are shown below (Brucker *et al.* 2007):

$$\zeta(\boldsymbol{x},t) = \frac{1}{N^3}\sum_{\boldsymbol{k}} \hat{\zeta}(\boldsymbol{k},t)\exp\left[I\left(k_i x_i - Stk_1x_2\right)\right], \tag{3.1}$$

$$\hat{\zeta}(\boldsymbol{k},t) = \sum_{\boldsymbol{x}} \zeta(\boldsymbol{x},t)\exp\left[-I\left(k_i x_i - Stk_1x_2\right)\right], \tag{3.2}$$

where $I \equiv \sqrt{-1}$. The cross term in the exponential Stk_1x_2 arises due to the shear-periodic boundary condition. As a consequence of this term, it is not possible to calculate the forward and reverse transforms using a standard three-dimensional fast Fourier transform (FFT).

Rogallo (1981) resolved this issue by transforming (2.3) into a coordinate system that deforms with the mean flow. In this moving frame of reference, the spectral transform reduces to the conventional three-dimensional FFT, allowing the use of a standard numerical algorithm. However, mean shear progressively distorts the mesh in physical space, leading to a growth in aliasing errors from the pseudo-spectral evaluation of the nonlinear terms on the deformed mesh. To relieve this problem, Rogallo introduced a remeshing step. As mentioned earlier, remeshing with dealiasing leads to a sudden loss in both the turbulent kinetic energy and turbulent energy dissipation rate.

We developed an alternate algorithm that works directly with (3.1) and (3.2) in the orthogonal (laboratory) frame of reference. The challenge was to accomplish the three-dimensional transform, with the phase shift, in $O(N^3 \ln N)$ operations, where N is the number of grid points in each direction. This was done by decomposing the three-dimensional transform into a sum of products of one- and two-dimensional transforms. To illustrate this point, we show the procedure for evaluating a forward transform.

The first step is to transform x_1, x_3 to k_1, k_3 by calling N two-dimensional real $\rightarrow$ complex FFTs yielding for an arbitrary physical-space variable $\phi(x_1, x_2, x_3)$:

$$\check{\phi}(k_1, x_2, k_3) = \sum_{x_1} \sum_{x_3} \phi(x_1, x_2, x_3) \exp\left[-I\,(k_1x_1 + k_3x_3)\right]. \tag{3.3}$$

We then phase shift the result to accommodate the uniform mean shear

$$\tilde{\phi}(k_1, x_2, k_3) \equiv \check{\phi}(k_1, x_2, k_3) \exp\left[I\,Stk_1x_2\right]. \tag{3.4}$$

The transform is completed by calling N^2 one-dimensional complex $\rightarrow$ complex FFTs to obtain

$$\hat{\phi}(k_1, k_2, k_3) = \sum_{x_2} \tilde{\phi}(k_1, x_2, k_3) \exp\left[-Ik_2x_2\right]. \tag{3.5}$$

The first calculation over planes will scale like $O(N \times N^2 \ln N)$ operations, the multiplication step $O(N^3)$, and the final transform over pencils like $O(N^2 \times N \ln N)$, yielding an overall scaling of $O(N^3 \ln N)$ operations.

We can similarly outline the reverse transform. The first step is to perform N^2 one-dimensional complex $\rightarrow$ complex pencil transformtions to obtain

$$\tilde{\phi}(k_1, x_2, k_3) = \frac{1}{N} \sum_{k_2} \hat{\phi}(k_1, k_2, k_3) \exp[Ik_2x_2]. \tag{3.6}$$

Next is the multiplication step:

$$\check{\phi}(k_1, x_2, k_3) \equiv \tilde{\phi}(k_1, x_2, k_3) \exp[-I\,Stk_1x_2], \tag{3.7}$$

followed by N two-dimensional complex $\rightarrow$ real, plane FFTs, yielding the desired transform

$$\phi(x_1, x_2, x_3) = \frac{1}{N^2} \sum_{k_1} \sum_{k_3} \check{\phi}(k_1, x_2, k_3) \exp\left[I\,(k_1x_1 + k_3x_3)\right]. \tag{3.8}$$

Again, the overall calculation scales as $O(N^3 \ln N)$ operations.

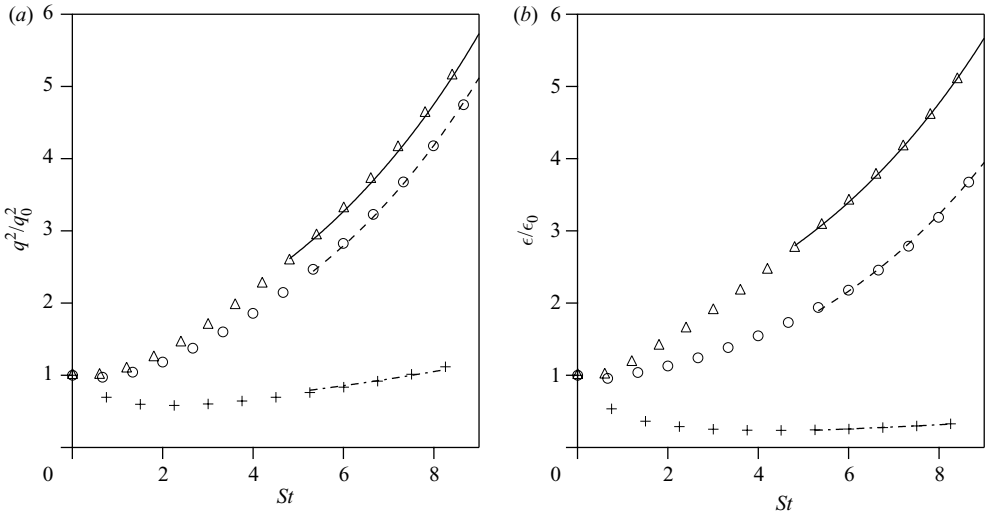

FIGURE 4. Time evolution of the normalized turbulent kinetic energy q^2/q_0^2 and normalized dissipation rate ϵ/ϵ_0 for + $S_0^* = 3$, ○ $S_0^* = 15$, and △ $S_0^* = 27$. Initial Reynolds number $(R_\lambda)_0 \sim 26$. The lines represent least squares fits to (3.9) and (3.10). The fitted values of σ are reported in table 1.

The approach is to solve the equations derived by Rogallo (1981) in Fourier space utilizing the above inverse transform to obtain the variables in physical space for the purpose of evaluating nonlinear products pseudo-spectrally. The algorithm has been implemented in a distributed computational environment using message passing interface (MPI). The data is decomposed into two-dimensional slabs that are distributed among the processors. Further details of the code and its validation against the Rogallo algorithm and experiments are discussed extensively in Brucker *et al.* (2007).

3.2. *DNS results*

DNS have been carried out at three values of the initial shear parameter $S_0^* = 3$, 15 and 27 and two initial Reynolds numbers $(R_\lambda)_0 = 26$ and 40. The results for the normalized turbulent kinetic energy q^2/q_0^2 and dissipation rate ϵ/ϵ_0 at the lower initial Reynolds number are shown in figure 4. The lines represent least squares fits to the expressions

$$q^2 = q_r^2 \exp\left[\sigma S (t - t_0)\right]. \tag{3.9}$$

$$\epsilon = \epsilon_r \exp\left[\sigma S (t - t_0)\right], \tag{3.10}$$

where q_r^2, ϵ_r, σ and t_0 are fitting parameters. In general, we observe exponential growth for both variables, with exponents that depend sensitively on the initial shear parameter (see table 1). The results are qualitatively consistent with earlier DNS (Lee *et al.* 1990) and experiments (Harris *et al.* 1977; Tavoularis & Corrsin 1981; Rohr *et al.* 1988; Tavoularis & Karnik 1989; DeSouza *et al.* 1995). Figure 5 shows the evolution of the Reynolds number and energy spectra for the lowest shear parameter. Once again, the growth in the Reynolds number is consistent with the earlier literature. The initial energy spectrum is defined in § 2.2. With time, the spectrum evolves in both directions as expected. We do not observe an inertial range in these simulations due

i–j	$\tilde{\Pi}_{ij}$	$\tilde{\epsilon}_{ij}$	b_{ij}	b_{ij} (2.13)	S_0^*	S^*	P/ϵ	σ (3.12)	σ (DNS fit)
1–2	0.156	−0.014	−0.165	−0.166	3	10.3	1.6	0.12	0.10
1–1	−0.090	0.082	0.154	0.168					
2–2	0.036	0.045	−0.137	−0.140					
3–3	0.054	0.068	−0.019	−0.028					
1–2	0.086	−0.004	−0.149	−0.159	15	19.6	2.8	0.19	0.20
1–1	−0.055	0.060	0.300	0.352					
2–2	0.021	0.015	−0.210	−0.208					
3–3	0.034	0.027	−0.092	−0.146					
1–2	0.050	−0.002	−0.126	−0.139	27	26.6	3.4	0.17	0.18
1–1	−0.031	0.049	0.391	0.484					
2–2	0.012	0.008	−0.255	−0.254					
3–3	0.019	0.018	−0.144	−0.229					

TABLE 1. Asymptotic values of $\tilde{\Pi}_{ij}$, $\tilde{\epsilon}_{ij}$, b_{ij}, S^*, P/ϵ and σ for each of the three values of S_0^*. The second column of b_{ij} is computed from (2.13). The first column of σ is obtained from (3.12) while the second column is determined by fitting the results shown in figure 4. Notice that the asymptotic value changes as a function of the initial shear parameter, and that the level of anisotropy of the flow decreases as the shear parameter increases.

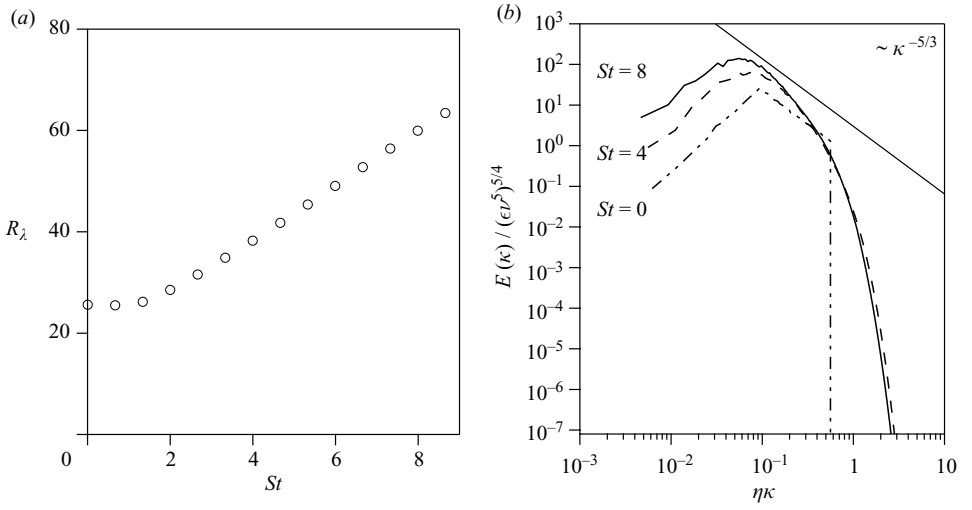

FIGURE 5. Time evolution of (*a*) R_λ and (*b*) the non-dimensional, three-dimensional energy spectrum, at the indicated values of St for $S_0^* = 27$ and $(R_\lambda)_0 = 26$.

to the modest Reynolds numbers (with the relatively strict resolution requirement we have adopted, as discussed in § 3.3).

Figure 6 shows the temporal evolution of the velocity derivative skewness M_3. The derivative skewness can be related to the turbulent energy cascade through the Kármán–Howarth equation (Pope 2000), and is therefore considered a measure of the degree to which the nonlinear terms have reached their equilibrium. We show results for initially Gaussian turbulence ($M_3(0) = 0$) subject to mean shear with $S_0^* = 3$, 15 and 27, and for isotropic turbulence that initially decayed until $M_3 \sim -0.4$ before being subjected to mean shear with $S_0^* = 3$ and 27. Following the application of mean shear, we observe M_3 decreases to a minimum and then slowly increases with time. The curves for the Gaussian turbulence, and for the isotropic turbulence that had decayed,

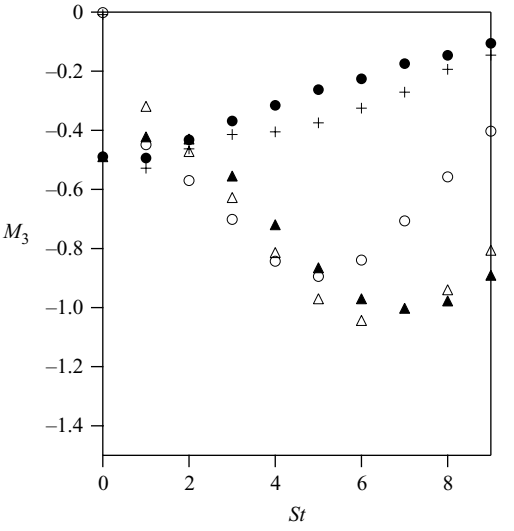

FIGURE 6. Time evolution of the skewness of the velocity derivative M_3 for Gaussian turbulence ($M_3(0) = 0$) with three initial values of the shear parameter: $S_0^* = 3$ +, 15 ○ and 27 △ and isotropic turbulence that initially decayed until $M_3 \sim -0.4$ and then was subjected to mean shear with $S_0^* = 3$ ● and 27 ▲.

approach each other by $St \sim 4$, suggesting little sensitivity to the initial skewness. The fact that M_3 reaches a minimum over the period of our simulations supports our contention that the nonlinear terms have had adequate time to equilibrate with the flow. The result is qualitatively consistent with the experimental data compiled by Tavoularis, Bennett & Corrsin (1978), who found $-M_3$ decreased with increasing Reynolds number over the range $10 \leqslant R_\lambda \lesssim 200$; however, their analysis considered only the Reynolds number, whereas the results in figure 6 show a clear dependence on the shear parameter as well. We interpret the minimum and subsequent growth of M_3 at longer times as an indication that classical energy transfer by the nonlinear terms is growing weaker with increasing St. Recall that energy also is being 'transferred' from low to high wavenumbers due to the linear stretching associated with the mean shear flow (Lumley 1964; Lumley & Panofsky 1964). Particularly at the higher values of the shear parameter, this linear transfer becomes the dominant mode of energy transfer, consistent with RDT. The results shown in figure 2 also support this view. The evolution of P/ϵ and S^* are only weakly affected by allowing the turbulence to decay initially so that M_3 approaches its equilibrium value of -0.4. Collectively, these results suggest that the dominant mechanism for energy transfer, particularly at larger values of S_0^*, is due to the linear stretching by the mean shear that is captured by RDT. This notion has been discussed by Lumley (1964) and Lumley & Panofsky (1964) for a boundary layer. The ultimate breakdown of RDT therefore involves other nonlinear effects that are discussed in § 4.3.

To quantitatively analyse the self-similar regime of HTSF, it is useful to consider non-dimensional quantities that approach an asymptote at long times. We then can study the dependence of the asymptotes on the two parameters (Reynolds number and shear parameter). Figure 7 shows the time evolution of S^* and P/ϵ from the DNS. As you can see, both quantities approach an asymptote that depends sensitively upon the initial value of S^*.

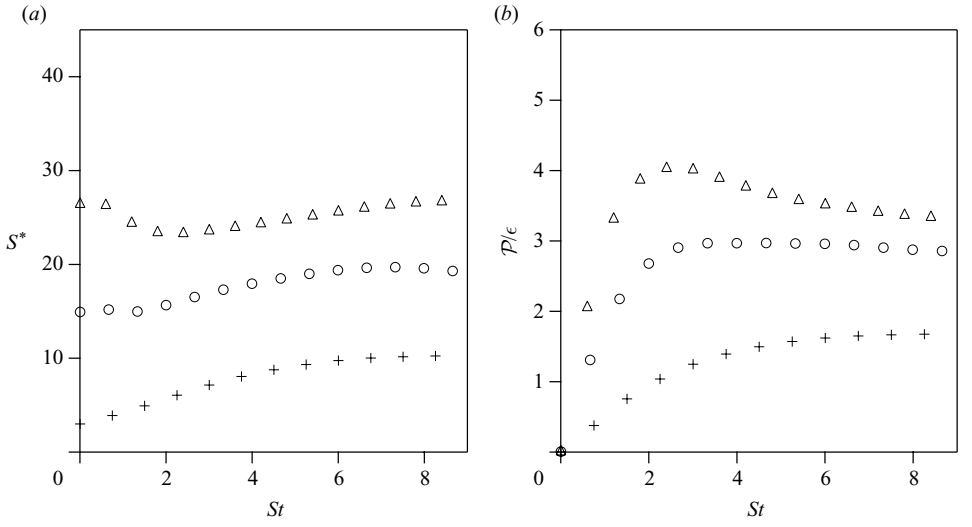

FIGURE 7. Time evolution of (*a*) the shear parameter S^* and (*b*) P/ϵ at + $S_0^* = 3$, ○ $S_0^* = 15$, and △ $S_0^* = 27$. The initial Reynolds number is $(R_\lambda)_0 \sim 26$. The asymptotic values are reported in table 1.

By definition we can write

$$b_{12} = \frac{P/\epsilon}{S^*}. \tag{3.11}$$

As P/ϵ and S^* approach constants at long times, (3.11) implies b_{12} will do the same. Figure 8 shows the four non-zero components of the anisotropic Reynolds stress tensor. Notice that each component approaches a constant at long times that depends on S_0^*. We can analyse the anisotropy of the turbulence by considering the invariants of the anisotropy tensor b_{ij}. The first invariant (the trace) is zero by definition. The second and third invariants are respectively: $II \equiv b_{ij}b_{ji}$ and $III \equiv b_{ij}b_{jk}b_{ki}$. If we then define $3\tilde{\eta}^2 = -2II$ and $2\xi^3 = III$, we can construct the evolution of the turbulence on the so-called 'Lumley triangle'. Figure 9 shows the evolution of the turbulence at the three values of the initial shear parameter. The vertices labelled $2C$ and $1C$ indicated two-component and one-component turbulence, respectively. Initially the curves begin at (0,0), corresponding to isotropic turbulence. The curves approach the $2C$ vertex at early times, but eventually come to a steady value (fixed point) near the $1C$ vertex, to a degree that increases with increasing initial shear parameter. Note that inviscid RDT predicts that the turbulence approaches the $1C$ vertex in the limit $St \to \infty$ (Pope 2000).

We further analyse the asymptotic behaviour of b_{ij} by seeking a steady state solution to (2.13). From the DNS we compute $\tilde{\Pi}_{ij}$ and $\tilde{\epsilon}_{ij}$ and solve (2.13) for b_{ij}, neglecting the transient term on the left-hand side. A summary of all of the terms, including a comparison of the prediction of (2.13) with the DNS asymptote taken from figure 8, is shown in table 1. Overall there is very good agreement between the two, moreover (2.13) captures all of the trends with S_0^* even though the time dependent term has been neglected. A similar result was obtained by Lee & Chung (1995), who solved model equations for b_{ij} and found that the steady state was sensitive to S_0^*. Note that these results are consistent with the exponential growth in q^2 and ϵ observed in figure 4. This can be seen by rewriting the turbulent kinetic energy equation (2.12) as

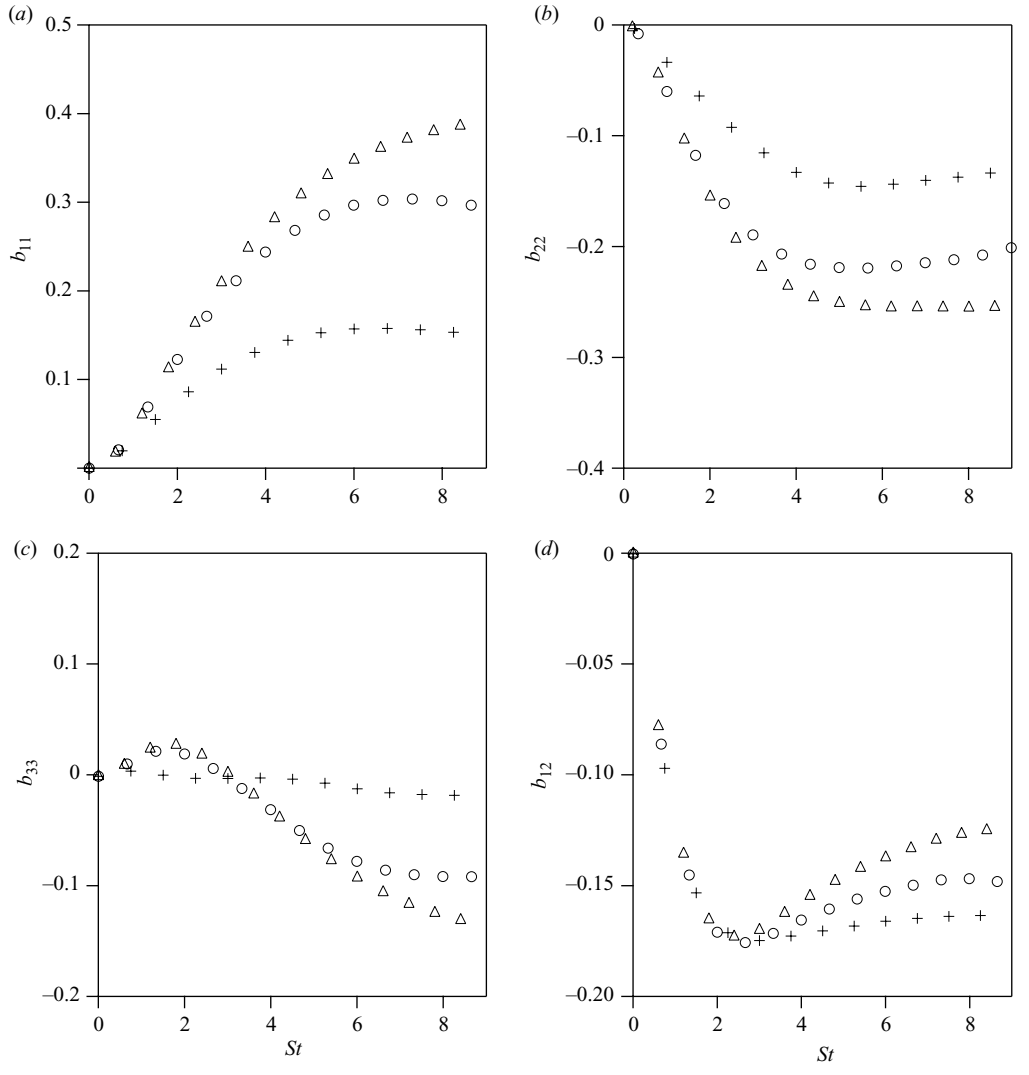

FIGURE 8. Time evolution of four components of the anisotropic Reynolds stress tensor: (*a*) $b_{11}(St)$; (*b*) $b_{22}(St)$; (*c*) $b_{33}(St)$; and (*d*) $b_{12}(St)$ at + $S_0^* = 3$, ○ $S_0^* = 15$ and △$S_0^* = 27$. Initial Reynolds number $(R_\lambda)_0 \sim 26$.

follows:

$$\frac{1}{Sq^2}\frac{\mathrm{d}q^2}{\mathrm{d}t} = 2b_{12}\left(\frac{\epsilon}{P} - 1\right) = \sigma. \tag{3.12}$$

As b_{12} and P/ϵ approach constants, we expect the same for σ, implying exponential growth of the turbulent kinetic energy at a rate that depends sensitively on S_0^*.

While the sensitivity to the shear parameter is evident in our results, we see very little sensitivity to the Reynolds number. Figure 10(*a*) shows a compilation of runs at $S_0^* = 3$ and 27 and $(R_\lambda)_0$ over the range 27–40. Here the results are somewhat less definitive because of the limited range of Reynolds number that we could sample (with our stringent resolution requirements). However, we note that a strong Reynolds number dependence would be inconsistent with a self-similar regime (with constant

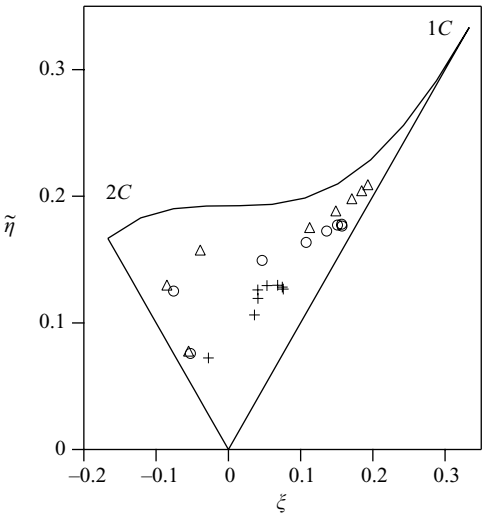

FIGURE 9. Plot of the Lumley triangle in the plane of invariants $(\tilde{\eta}, \xi)$ of the Reynolds stress anisotropy tensor. The vertices correspond to two-component $(2C)$ and one-component $(1C)$ turbulence, as indicated. The points correspond to $S_0^* = 3$ +, $S_0^* = 15$ ○ and $S_0^* = 27$ △, with an initial Reynolds number $(R_\lambda)_0 \sim 26$. Notice the points appear to approach a constant fixed point that depends on the initial shear parameter.

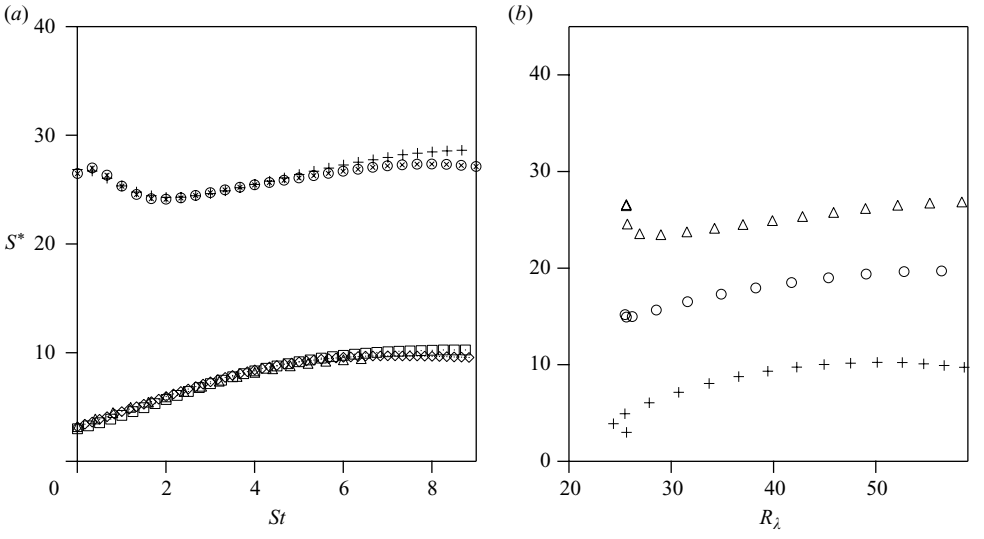

FIGURE 10. (*a*) Effect of initial Reynolds number on the asymptotic value of S^* for two initial values of S_0^*. ⊡ $(R_\lambda)_0 = 27$, ◇ $(R_\lambda)_0 = 33$, △ $(R_\lambda)_0 = 40$, ⊗ $(R_\lambda)_0 = 30$ and + $(R_\lambda)_0 = 26$. (*b*) Parameter plot S^* versus R_λ for the three different shear rates.

σ) since the Reynolds number grows with increasing St (see figure 5*a*). Figure 10(*b*) shows the same data in the form of a parameter: S^* versus R_λ. The nearly horizontal lines at the three values of S^* are consistent with the apparent weak Reynolds number dependence. We do point out that there might be a 'threshold' Reynolds number that must be exceeded to achieve self-similarity. In DNS done at very low shear parameter

(not shown), we observed the turbulence decays (i.e. $\sigma < 0$). It's possible this is linked to the relatively small initial Reynolds number in our DNS. That is, if the initial Reynolds number is so small that the nonlinear interactions are negligible by the time the DNS has achieved appreciable strain (say $St \sim 1$), the system cannot initiate exponential growth of the kinetic energy.

3.3. *Discussion of DNS results*

The conclusions drawn in §3.2 are not completely consistent with some earlier DNS results. For example, Yu & Girimaji (2005) found that the asymptotes for the turbulence statistics in their flow were insensitive to the initial shear parameter. Shih *et al.* (2000) concluded there are three regimes: (i) at low Reynolds numbers, HTSF is sensitive to the shear parameter and the Reynolds number; (ii) at intermediate Reynolds numbers, HTSF is sensitive to the Reynolds number and is independent of the shear parameter and (iii) at very high Reynolds numbers, HTSF is independent of both the shear parameter and the Reynolds number. Jacobitz *et al.* (1997) found that the large-scale turbulence statistics are independent of Reynolds number for the higher Reynolds numbers in their study, but they identified three regimes for the shear parameter: (i) at low S_0^* the turbulence decays (i.e. $\sigma < 0$); (ii) at moderate S_0^* the turbulence grows exponentially; and (iii) for $S_0^* > 6$ the turbulence decays. Similar results were reported by Jacobitz & Sarkar (1999).

The origin of these discrepancies is not clear. However, we have discovered that an important consideration with all HTSF simulations is numerical resolution. The difficulty arises from the fact that the integral length scale L_{11} increases and the Kolmogorov length $\eta \equiv (\nu^3/\epsilon)^{1/4}$ decreases in time (see figure 5). Hence, DNS can only observe a finite window of time (currently $St \leqslant 10$) before loss of resolution at the large and/or small scales causes the simulation to fail. Ideally DNS should fail at the large and small scales simultaneously, as this maximizes the temporal window of the simulation. We have chosen the peak wavenumber κ_0 and the fluid viscosity ν to control the initial value of the longitudinal length scale and the Kolmogorov scale respectively (see (2.5)) so that the near ideal simulation is achieved. At the large scale, we monitor L_{11}/L, where $L = 2\pi$ is the box size, to make sure the large scales are well resolved. We initially considered the large scales well resolved when $L_{11}/L \leqslant 0.1$. However, we also track the slope $\mathrm{d}L_{11}/\mathrm{d}t$, which we expect to be positive, based on the arguments presented earlier. At the small scale we track $k_{max}\eta$, where k_{max} is the maximum resolved wavenumber, as a measure of the resolution of the small scales. The DNS is considered resolved when $k_{max}\eta \geqslant 1$. Figure 11 demonstrates the importance of maintaining resolution of the small scales. Notice that at the moment that the condition is violated the asymptotic value of S^* is lost. We attribute the deviation from the asymptote to loss of resolution of the large and/or small scales. This may explain at least some of the discrepancies in the literature. For example, the study by Shih *et al.* (2000) that found no dependence on the shear parameter was done at much lower resolution (grid size of 128^3) and yet had higher Reynolds numbers than the present study.

A second complication with some of the numerical studies is the use of flows that are not precisely HTSF. For example, the simulation of Schumacher (2004) that imposes a linear body force produces a flow that is similar to, but not precisely the same as HTSF. This is especially true for the large scales, that in their flow achieve a steady state with $P/\epsilon = 1$, while we observe indefinite growth, corresponding to $P/\epsilon > 1$. The simulation of Yu & Girimaji (2005) too is not strictly HTSF. They studied Couette flow and restricted their attention to the centre of the channel where

Reference	b_{12}	S^*	St
Tavoularis & Karnik (1989)	−0.16	8.6	10–28
Tavoularis & Corrsin (1981)	−0.14	12.5	8–12
DeSouza *et al.* (1995)	−0.11	21.8	11–16

TABLE 2. Asymptotic values of b_{12} and S^* for the indicated homogeneous shear flow experiments. Notice that the asymptotic value changes as a function of the shear parameter, and that the anisotropy of the flow decreases as the asymptotic value of the shear parameter increases. The fourth column (St) indicates the duration of time the asymptotic level was observed.

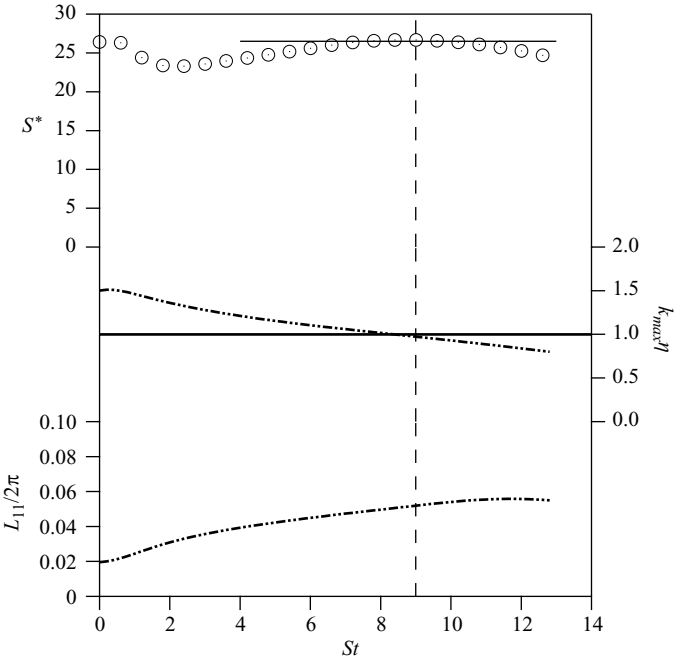

FIGURE 11. Effect of under-resolution at the small scales on the asymptotic value of S^*.

the turbulence is nearly homogeneous. Nevertheless, there are aspects of this flow that will systematically deviate from HTSF, particularly when considering the long-time asymptote, as Couette flow will eventually approach a steady state. In our opinion, it is not straightforward to know when these slight deviations from true HTSF will begin to affect the dynamics of the large scales.

Given the conflicts in the DNS literature, we seek further evidence from experiments to support our findings. The work of Tavoularis (Tavoularis & Corrsin 1981; Tavoularis & Karnik 1989; DeSouza *et al.* 1995) spans the broadest range of the shear parameter. The asymptotic values reported in these studies show a systematic dependence of the long-time asymptotes of b_{12} on the shear parameter. Table 2 shows a compilation of their results, along with the range of St that was observed in their wind tunnel. The asymptotes are in quantitative agreement with the values found from DNS (see table 1), supporting our conclusion about the importance of S_0^*, and implicitly confirming the conclusion about the insensitivity to the Reynolds number, which varies strongly along the length of the wind tunnel.

4. Rapid distortion theory

As suggested by Townsend (1976), Hunt & Carruthers (1990), Lee *et al.* (1990), Rogers (1991) and others, when the mean deformation rate is large compared to the turbulence time scales (i.e. $S^* \gg 1$), (2.3) can be linearized by neglecting turbulence–turbulence interactions. Solutions to the linearized equations are often referred to as RDT. The most commonly used form of the theory is based on the Euler equations, where the viscous terms also have been neglected. We shall refer to this as inviscid RDT or '*i*RDT'. The justification often made for neglecting the viscous terms is that, in the absence of the nonlinear terms that are responsible for the energy cascade, the viscous terms are expected to be negligible. The resulting solution of the *i*RDT equations for the velocity (and all related turbulence statistics) depends solely on the total strain $\beta \equiv St$, and is independent of the shear rate (so long as it is large enough to justify the RDT assumptions).

Our objective here is to understand the relevance of the initial Reynolds number and shear parameter, both of which depend upon the energy dissipation rate. *i*RDT cannot be used to consider this question. Instead, we analyse the RDT approximation to the full Navier–Stokes equation that includes the viscous terms (referred to hereafter as '*v*RDT'). As the viscous terms are linear, the resulting solution remains analytic, and is only slightly more complex than *i*RDT.

4.1. *Basic formulation*

The *v*RDT equations can be solved in Fourier space yielding (Moffat 1967; Townsend 1970; Maxey 1982; Rogers 1991)

$$\hat{\boldsymbol{u}}'(\boldsymbol{k}, t) = \exp(-\Gamma)\, \boldsymbol{A} \cdot \hat{\boldsymbol{u}}'(\boldsymbol{k}_0, 0), \tag{4.1}$$

where $\hat{\boldsymbol{u}}'(\boldsymbol{k}, t)$ is the Fourier transform of the fluctuating velocity at time t, given the initial velocity $\hat{\boldsymbol{u}}'(\boldsymbol{k}_0, 0)$. Note that the mean shear causes the wavevector $\boldsymbol{k}$ to be a function of time. If we define the initial wavevector as $\boldsymbol{k}_0 \equiv (k_1, k_2, k_3)$, the wavevector at time t is given by $\boldsymbol{k} \equiv (k_1, k_2 - k_1 St, k_3)$. Γ and the transformation matrix $\boldsymbol{A}$ are defined as

$$\Gamma = \nu t \left[k_0^2 - k_1 k_2 St + \frac{(k_1 St)^2}{3} \right], \tag{4.2}$$

$$\boldsymbol{A}(\boldsymbol{k}, t) = \begin{bmatrix} 1 & \frac{k_0^2}{(k_1^2 + k_3^2)} \left(-\frac{k_3^2}{k_0^2} P + \frac{k_1^2}{k_0^2} Q \right) & 0 \\ 0 & \frac{k_0^2}{k^2} & 0 \\ 0 & \frac{k_1 k_3}{(k_1^2 + k_3^2)} (P + Q) & 1 \end{bmatrix}, \tag{4.3}$$

where $k_0^2 \equiv \boldsymbol{k}_0 \cdot \boldsymbol{k}_0$, $k^2 \equiv \boldsymbol{k} \cdot \boldsymbol{k}$ and the functions P and Q are given by

$$P = \frac{k_0^2}{k_1 \sqrt{k_1^2 + k_3^2}} (\arctan \alpha - \arctan \tau), \tag{4.4}$$

$$Q = \frac{St \left(k_0^2 - 2k_2^2 + k_1 k_2 St \right)}{k^2}. \tag{4.5}$$

The angles α and τ are

$$\alpha = \frac{k_2}{\sqrt{k_1^2 + k_3^2}}, \quad \tau = \frac{k_2 - k_1 St}{\sqrt{k_1^2 + k_3^2}}. \tag{4.6}$$

The above expressions allow us to evolve forward an arbitrary initial spectral velocity, $\hat{\boldsymbol{u}}'(\boldsymbol{k}_0, 0)$. The initial velocity is assumed to be isotropic and Gaussian, with a three-dimensional velocity spectrum defined as

$$\Phi_{ij}^0(\boldsymbol{k}_0, 0) = \frac{E_0(k_0)}{4\pi k_0^2}\left(\delta_{ij} - \frac{k_i k_j}{k_0^2}\right), \tag{4.7}$$

where $E_0(k_0)$ is the initial energy spectrum. The three-dimensional spectrum at time t is then obtained from the following mapping

$$\Phi_{ij}(\boldsymbol{k}, t) = e^{(-2\Gamma)} A_{ip} A_{jq} \Phi_{pq}^0(\boldsymbol{k}_0, 0). \tag{4.8}$$

Arbitrary single-point statistics are determined from integrals of the spectrum, for example,

$$R_{ij}(t) = \iiint D_v A_{ip} A_{jq} \Phi_{ij}^0(\boldsymbol{k}_0, 0)\,\mathrm{d}\boldsymbol{k}, \tag{4.9}$$

$$\epsilon(t) = 2\nu \iiint k^2 D_v A_{ip} A_{iq} \Phi_{ij}^0(\boldsymbol{k}_0, 0)\,\mathrm{d}\boldsymbol{k}, \tag{4.10}$$

$$\begin{aligned} \Pi_{ij}^{\mathrm{r}} &= \overline{\frac{p^r}{\rho}\left(\frac{\partial u_i'}{\partial x_j} + \frac{\partial u_j'}{\partial x_i}\right)} \\ &= -2S \iiint \left[\frac{k_i k_1}{k^2}\Phi_{j2}(\boldsymbol{k}, t) + \frac{k_j k_1}{k^2}\Phi_{i2}(\boldsymbol{k}, t)\right] \mathrm{d}\boldsymbol{k}, \end{aligned} \tag{4.11}$$

where p^r is the solution to (2.4) based on the 'rapid' term only and $D_v \equiv \exp(-2\Gamma)$. These relationships will be used to predict the evolution of various large-scale, single-point quantities that will be compared to the DNS results.

4.2. *Viscous RDT at short times*

The initial development of the turbulence can be analysed analytically by performing an asymptotic expansion of the vRDT solution (4.9) and (4.10) in the limit $\beta \equiv St \to 0$. We begin by defining the nth moment of the initial energy spectrum as

$$\frac{I_n}{2} = \nu^n \int_0^\infty k^{2n} E_0(k_0)\,\mathrm{d}k_0. \tag{4.12}$$

The initial turbulent kinetic energy and dissipation rate are then $q_0^2 = I_0$ and $\epsilon_0 = I_1$ respectively. Using (4.9) and (4.10), we obtain the following evolution equations for the kinetic energy and dissipation rate

$$\frac{q^2}{q_0^2}(\beta) \sim 1 - \frac{2}{S_0^*}\beta + \left(\frac{2}{15} + 2M_2\right)\beta^2 + \left(-\frac{4}{3}M_3 - \frac{16}{45}\frac{1}{S_0^*}\right)\beta^3 + \left(\frac{2}{3}M_4 + \frac{26}{45}M_2\right)\beta^4 + \cdots, \tag{4.13a}$$

$$\begin{aligned} \frac{\epsilon}{\epsilon_0}(\beta) \sim 1 - 2N_2\beta + \left(\frac{1}{3} + 2N_3\right)\beta^2 + \left(-\frac{4}{3}N_4 - \frac{46}{45}N_2\right)\beta^3 \\ + \left(\frac{1}{105} + \frac{2}{3}N_5 + \frac{68}{45}N_3\right)\beta^4 + \cdots, \end{aligned} \tag{4.13b}$$

where $M_n \equiv I_n/(q_0^2 S^n)$ and $N_n \equiv I_n/(\epsilon_0 S^{n-1})$. The equations for P/ϵ and S^* are

$$\begin{aligned}\frac{P}{\epsilon}(\beta) \sim{}& \frac{2}{15}S_0^*\beta + \left(-\frac{1}{5} + \frac{4}{15}N_2 S_0^*\right)\beta^2 \\ &+ \left(-\frac{2}{5}N_2 + \frac{8}{15}N_2^2 S_0^* + \frac{2}{15}M_2 S_0^* - \frac{4}{15}N_3 S_0^* - \frac{2}{45}S_0^*\right)\beta^3 \\ &+ \left(\frac{2}{45} - \frac{4}{5}N_2^2 + \frac{2}{3}N_3 - \frac{2}{45}M_3 S_0^* - \frac{28}{675}N_2 S_0^* + \frac{4}{15}M_2 N_2 S_0^*\right. \\ &\left. + \frac{16}{15}N_2^3 S_0^* - \frac{16}{15}N_2 N_3 S_0^* + \frac{8}{45}N_4 S_0^*\right)\beta^4 + \cdots, \end{aligned} \tag{4.14a}$$

$$\begin{aligned} S^*(\beta) \sim{}& S_0^* + \left(-2 + 2N_2 S_0^*\right)\beta \\ &+ \left(-4N_2 - \frac{1}{5}S_0^* + 2M_2 S_0^* + 4N_2^2 S_0^* - 2N_3 S_0^*\right)\beta^2 \\ &+ \left(\frac{14}{45} - 8N_2^2 + 4N_3 - \frac{4}{3}M_3 S_0^* - \frac{2}{45}N_2 S_0^* + 8N_2^3 S_0^* - 8N_2 N_3 S_0^* + \frac{4}{3}N_4 S_0^*\right)\beta^3 \\ &+ \left(-\frac{4}{45}N_2 - 16N_2^3 + 16N_2 N_3 - \frac{8}{3}N_4 + \frac{4}{45}M_2 S_0^* + \frac{2}{3}M_4 S_0^* - \frac{8}{3}M_3 N_2 S_0^*\right. \\ &+ \frac{28}{45}N_2^2 S_0^* + 8M_2 N_2^2 S_0^* + 16N_2^4 S_0^* - \frac{4}{9}N_3 S_0^* - 4M_2 N_3 S_0^* \\ &\left. - 24N_2^2 N_3 S_0^* + 4N_3^2 S_0^* + \frac{16}{3}N_2 N_4 S_0^* - \frac{2}{3}N_5 S_0^* + \frac{2}{35}S_0^*\right)\beta^4 + \cdots. \end{aligned} \tag{4.14b}$$

The expansions reveal an explicit dependence of all turbulence statistics on S_0^* and an implicit dependence on the shape of the initial energy spectrum (and hence R_λ) through the integrals I_n. Figure 12 shows a comparison between the DNS and vRDT solutions for P/ϵ. The expansion captures the early time development well ($St \lesssim 2$), particularly at the higher value initial shear parameter, which is consistent with the underlying assumptions of the theory.

We also can derive analytical expressions for the anisotropic Reynolds stress tensor

$$\begin{aligned}\frac{R_{11}}{q_0^2}(\beta) \sim{}& \frac{1}{3} - \frac{2}{3}\frac{1}{S_0^*}\beta + \left(\frac{2}{21} + \frac{2}{3}M_2\right)\beta^2 + \left(-\frac{4}{9}M_3 - \frac{68}{315}\frac{1}{S_0^*}\right)\beta^3 \\ &+ \left(-\frac{1}{1485} + \frac{2}{9}M_4 + \frac{88}{315}M_2\right)\beta^4 + \cdots, \end{aligned} \tag{4.15a}$$

$$\begin{aligned}\frac{R_{22}}{q_0^2}(\beta) \sim{}& \frac{1}{3} - \frac{2}{3}\frac{1}{S_0^*}\beta + \left(-\frac{4}{105} + \frac{2}{3}M_2\right)\beta^2 + \left(-\frac{4}{9}M_3 + \frac{44}{315}\frac{1}{S_0^*}\right)\beta^3 \\ &+ \left(\frac{3}{385} + \frac{2}{9}M_4\beta^4 + \frac{52}{315}M_2\right)\beta^4 + \cdots, \end{aligned} \tag{4.15b}$$

$$\begin{aligned}\frac{R_{33}}{q_0^2}(\beta) \sim{}& \frac{1}{3} - \frac{2}{3}\frac{1}{S_0^*}\beta + \left(\frac{8}{105} - \frac{2}{3}M_2\right)\beta^2 + \left(-\frac{4}{9}M_3 - \frac{88}{315}\frac{1}{S_0^*}\right)\beta^3 \\ &+ \left(-\frac{74}{10395} + \frac{2}{9}M_4\beta^4 + \frac{146}{315}M_2\right)\beta^4 + \cdots, \end{aligned} \tag{4.15c}$$

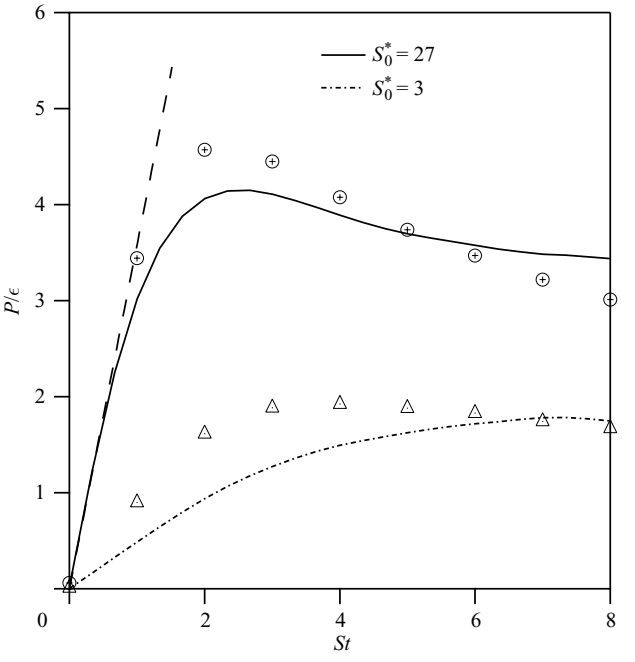

FIGURE 12. Comparison of the time evolution P/ϵ from vRDT (markers) and DNS (lines) for the indicated initial values of S_0^* and $(R_\lambda)_0 \sim 26$. The dashed lines shows the expansion given by (4.14*a*).

$$\frac{R_{12}}{q_0^2}(\beta) \sim \frac{2}{15}\beta - \frac{1}{5}\frac{1}{S_0^*}\beta^2 + \frac{2}{15}M_2\beta^3 - \left(\frac{2}{45}M_3 + \frac{1}{45}\frac{1}{S_0^*}\right)\beta^4 - \left(\frac{188}{135135} - \frac{2}{45}M_2\right)\beta^5 + \cdots . \quad (4.15d)$$

Notice that setting $M_n = 0$ and $S_0^* = \infty$ the above equations reduce to the inviscid expansions derived by Rogers (1991).

4.3. *Viscous RDT at long times*

It is not possible to derive an analytical solution to the vRDT equations that is valid for all time. Instead we must numerically evaluate the integrals shown in (4.9)–(4.11). The integrals are most easily computed in spherical coordinates, with the axis oriented such that $k_1 = k\cos\theta$, $k_2 = k\sin\theta\sin\phi$, $k_3 = k\sin\theta\cos\phi$ and $\mathrm{d}\boldsymbol{k} = k^2\sin\theta\mathrm{d}k\mathrm{d}\theta\mathrm{d}\phi$. To improve the accuracy of the numerical integration, it is convenient to replace the initial energy spectrum with an exponential function of the following form

$$E_0(k_0) = c_1 k_0^2 \exp\left(-c_2 k_0^2\right), \quad (4.16)$$

where c_1 and c_2 are adjustable parameters. Using this form of the spectrum, it is possible to analytically evaluate the semi-infinite integrals over the wavenumber k (Thacker *et al.* 1999). Numerical integration is then only required over the angles θ and ϕ. The numerical integrals were performed using a two-dimensional Simpson's rule (Press *et al.* 1999). The angular grid was refined until convergence was achieved. To test the accuracy of our numerical scheme, we show in figure 13 a comparison between the asymptote for $R_{22}(\beta)/q_0^2$ and $R_{12}(\beta)/q_0^2$ in the limit $\beta \to \infty$ for the

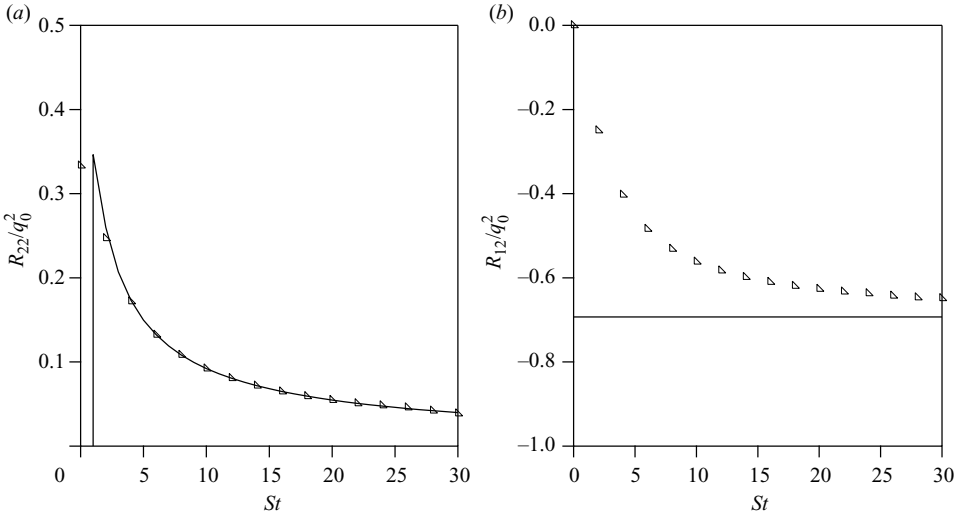

FIGURE 13. Test of the numerical scheme for evaluating the integrals at long times. (*a*) Comparison of numerical evaluation of *inviscid* RDT equations (markers) for R_{22} with the asymptotic prediction (lines) $\ln(4\beta)/(4\beta)$ of Rogers (1991). (*b*) Comparison of R_{12} with the asymptotic prediction of $-\ln(2)$ also by Rogers (1991).

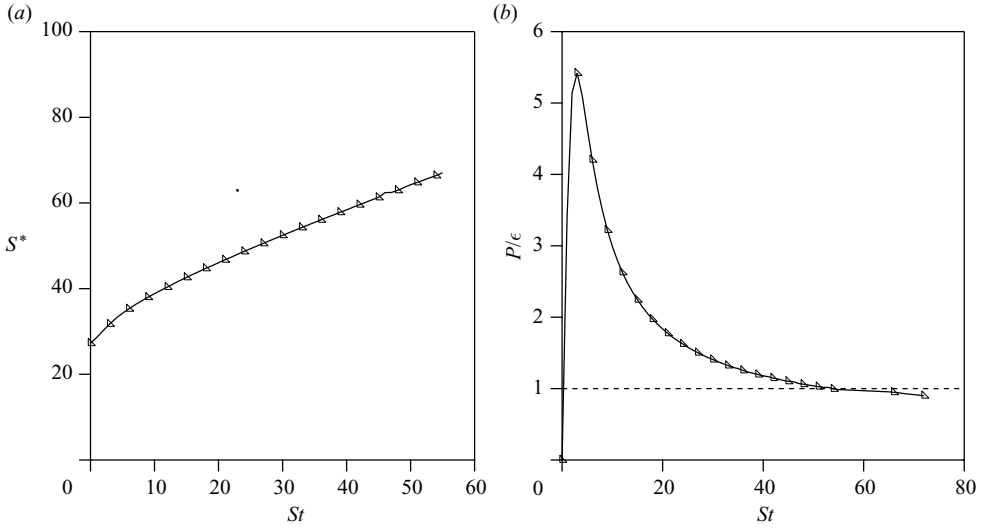

FIGURE 14. Time evolution S^* and P/ϵ from vRDT for an initial value of $S_0^* = 27$ and $R_\lambda \sim 26$. Notice that P/ϵ goes below one showing that the turbulence will decay at long times.

inviscid case (i.e. $\nu = 0$) that was derived by Rogers (1991) with the numerical results (symbols). The good agreement confirms the numerical procedure.

Figure 14 shows the evolution of S^* and P/ϵ predicted by vRDT for $0 \leqslant St \leqslant 80$. We see that vRDT predicts indefinite growth of S^*, but that $P/\epsilon < 1$ at long times and hence the eventual decay of the turbulence (i.e. $\sigma < 0$ for $\beta \to \infty$). It also predicts $b_{12} \to 0$ at long times (see figure 15) making the production term in the turbulent kinetic energy balance equation approach zero. These long-time predictions are inconsistent with most DNS and virtually all of the experiments. Interestingly,

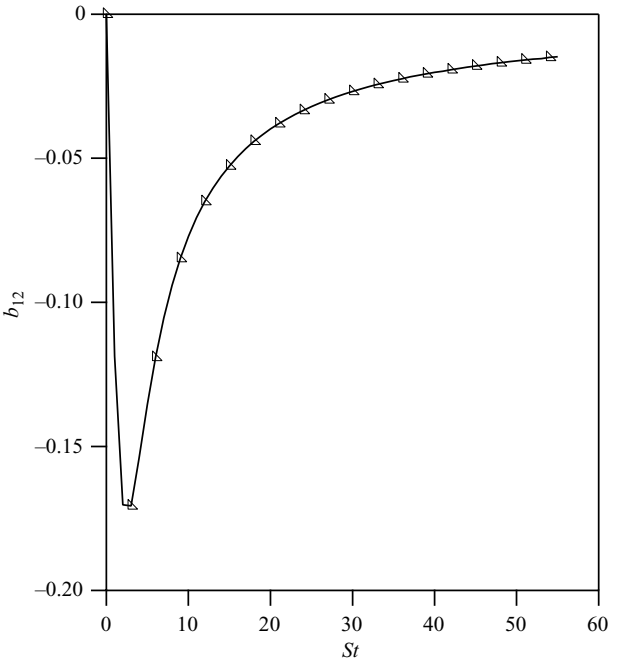

FIGURE 15. Time evolution b_{12} from vRDT for an initial value of $S_0^* = 27$ and $R_\lambda \sim 26$.

the predicted growth of S^* with time superficially strengthens the assumptions of the theory, making the cause for its breakdown at long times unclear.

Clues to the cause of the failure of the theory can be found by considering the balance equation for R_{22} (2.7*b*). The only source for this component of the Reynolds stress is due to the pressure–strain term Π_{22}. Recalling that only the 'rapid' terms are retained in vRDT (see (4.11)) we can write

$$\Pi_{22}^r = -2S \iiint \exp\left[-2\frac{\beta\nu}{S}\left(k_0^2 - \beta k_1 k_2 + \frac{\beta^2 k_1^2}{3}\right)\right] \times E_0(k_0)\,\frac{(k_2 - \beta k_1)\,k_1\left(k_1^2 + k_3^2\right)}{4\pi\left(k_0^2 + \beta^2 k_1^2 - 2\beta k_1 k_2\right)^3}\,\mathrm{d}\boldsymbol{k}. \quad (4.17)$$

The integrand of (4.17) goes to zero as $\beta \to \infty$ due to the unbounded (negative) growth of the exponent and the term in the denominator: $k_0^2 + \beta^2 k_1^2 - 2\beta k_1 k_2$. Consequently, vRDT predicts $R_{22} \to 0$ at long times. Figure 16 shows that the rapid term is initially negative (a sink) and approaches zero at long times. The resulting two-dimensional turbulence has no sources for any of the components of the Reynolds stress, and so they all eventually decay (figure 15). We define the 'slow' pressure–strain correlation as

$$\Pi_{ij}^s \equiv \overline{\frac{p^s}{\rho}\left(\frac{\partial u_i'}{\partial x_j} + \frac{\partial u_j'}{\partial x_i}\right)}, \quad (4.18)$$

where p^s refers to the solution of the Poisson equation for the pressure (2.4) based solely on the slow term on the right-hand side. In figure 16, we see that the rapid and slow contributions to the same component of the pressure–strain correlation behave differently. The nonlinear slow term acts as a *source* of R_{22} that eventually causes the rapid term to change sign and become a source as well. Thus, the slow pressure–strain

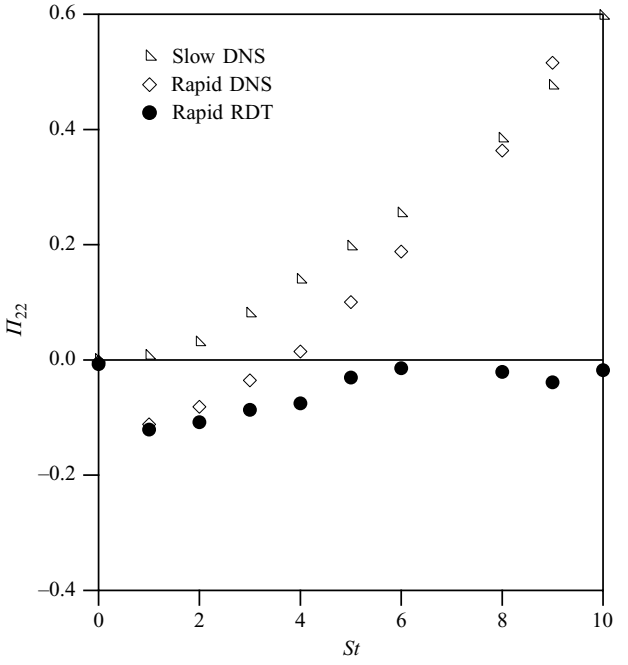

FIGURE 16. Time evolution of the rapid pressure–strain correlation Π^r_{22} (see (4.11) for the definition) from DNS and vRDT, and the slow pressure–strain correlation Π^s_{22} (see (4.18) for the definition) from DNS for $S^*_0 = 27$ and $R_\lambda \sim 26$.

term Π^s_{22} is essential for sustaining the three-dimensionality of the turbulence that enables the source terms to exceed the sinks and the turbulence to grow indefinitely (Deissler 1970). These results suggest a simple fix of vRDT at long times may be the introduction of a nonlinear model for Π^s_{22}, such as the pressure–strain model of Rotta (1951).

5. Conclusions

In this study, we investigated the asymptotic behaviour of HTSF using a combination of DNS and viscous RDT. The DNS was performed using a code that allows the shear rate to be varied over a wide range (Brucker *et al.* 2007). Over the window of time that the simulations retain good resolution of large and small scales, DNS predicts the large scales approach a self-similar state that is sensitive to the initial value of the shear parameter S^*_0, and insensitive to the initial Reynolds number. The results are consistent with the body of work by Tavoularis and coworkers that showed a similar dependence of the self-similar regime on the shear parameter, and (implicitly) no sensitivity to the Reynolds number that was growing along the length of the wind tunnel. There remain inconsistencies with earlier DNS studies that we cannot fully explain. We demonstrated the importance of grid resolution and note that some of these studies may have suffered from insufficient grid resolution (based on the size of the grid and the value of the Reynolds number in the simulation). Unfortunately, all DNS studies have this potential effect coming into play. To minimize this possibility, we implemented stringent resolution requirements that ultimately limited the range of Reynolds numbers that could be achieved ($26 \leqslant R_\lambda \leqslant 63$). The relative insensitivity

to Reynolds number gives us confidence that these results are general and not an artifact of the moderate Reynolds numbers in the study.

Following earlier investigations, we analysed the short and long-term behaviour of shear flow using RDT. The analytical solution to vRDT for short times is in excellent agreement with the DNS at high values of the shear parameter. The results show how S_0^* and R_λ enter into the solution. Analysing this result helps explain the strong sensitivity of the large-scale turbulence statistics to the shear parameter and the weak sensitivity to the Reynolds number (the dependence on R_λ enters implicitly through its effect on the spectral moments I_n). Numerical evaluation of the vRDT integrals for long times, however, yields results that are completely inconsistent with the DNS and experiments. In particular, the turbulent kinetic energy and viscous dissipation rate are found to decay to zero at long times. The cause has been traced to the pressure–strain terms for the velocity component in the shear direction. The rapid component initially acts as a sink term, as does viscous dissipation. In the absence of the 'slow' component arising from the nonlinear convective terms, vRDT predicts this component of the Reynolds stress decays to zero. The other components of the Reynolds stress then have no source term and so they all decay. In the DNS, the 'slow' pressure–strain term counteracts this tendency, eventually causing the rapid term to change sign. The two pressure–strain terms, acting together as sources, maintain the three-dimensionality of the turbulence, thereby allowing for the indefinite growth of all components of the Reynolds stress tensor. This suggests a simple fix of the theory, namely, to include a model for the nonlinear pressure–strain term acting in the shear direction.

The high degree of sensitivity of the outcome of HTSF to small changes in the relative size of the components of the Reynolds stress may explain why the long-time asymptotic behaviour remains so controversial.

The authors thank Z. Warhaft and K. A. Brucker for their valuable input. This work was supported by the National Science Foundation under grants PHY-0554675 and CBET-0756510. Juan C. Isaza was partially supported by a fellowship from the Fulbright Commission.

Note added in proof: Recently we have conducted experimental measurements of HTSF in a wind tunnel that extend the range of the Reynolds number ($100 < (R_\lambda)_0 < 250$) and the maximum time ($0 < St < 20$). The results are consistent with the findings reported here, i.e., the asymptotic state of the large-scale turbulence statistics is a strong function of the initial value of the shear parameter, but not of the initial value of the Reynolds number. Details can be found in Isaza, Warhatt & Collins (2009).

REFERENCES

Brucker, K. A., Isaza, J. C., Vaithianathan, T. & Collins, L. R. 2007 Efficient algorithm for simulating homogeneous turbulent shear flow without remeshing. *J. Comput. Phys.* **225**, 20–32.

Champagne, F. H., Harris, G. V. & Corrsin, S. 1970 Experiments on nearly homogeneous turbulent shear flow. *J. Fluid Mech.* **41**, 81–139.

Deissler, R. G. 1961 Effects of inhomogeneity and of shear flow in weak turbulent fields. *Phys. Fluids* **4** (10), 1187–1198.

Deissler, R. G. 1970 Effect of initial condition on weak homogeneous turbulence with uniform shear. *Phys. Fluids* **13** (7), 1868–1869.

DeSouza, F. A., Nguyen, V. D. & Tavoularis, S. 1995 The structure of highly sheared turbulence. *J. Fluid Mech.* **303**, 155–167.

Ferchichi, M. & Tavoularis, S. 2000 Reynolds number effect on the fine structure of uniformly sheared turbulence. *Phys. Fluids* **12** (11), 2942–2953.

Fox, J. 1964 Velocity correlations in weak turbulent shear flow. *Phys. Fluids* **7** (4), 562–564.

Garg, S. & Warhaft, Z. 1998 On small scale statistics in a simple shear flow. *Phys. Fluids* **10**, 662–673.

Harris, G. V., Graham, A. J. & Corrsin, S. 1977 Further experiments in nearly homogeneous shear flow. *J. Fluid Mech.* **81**, 657–687.

Hunt, J. C. R. & Carruthers, D. J. 1990 Rapid distortion theory and the problems of turbulence. *J. Fluid Mech.* **212**, 497–532.

Isaza, J. C., Warhatt, W. & Collins, L. R. 2009 Experimental investigation of the large-scale velocity statistics in homogeneous turbulent shear flow. *Phys. Fluids*, in press.

Jacobitz, F. G. & Sarkar, S. 1999 On the shear number effect in stratified shear flow. *Theor. Comput. Fluid Dyn.* **13** (3), 171–188.

Jacobitz, F. G., Sarkar, S. & van Atta, C. W. 1997 Direct numerical simulations of the turbulence evolution in a uniformly sheared and stably stratified flow. *J. Fluid Mech.* **342**, 231–261.

Lee, W. G. & Chung, M. K. 1995 The equilibrium states and the stability analysis of Reynolds stress equations for homogeneous turbulent shear flows. *Phys. Fluids* **7** (11), 2807–2819.

Lee, M. J., Kim, J. & Moin, P. 1990 Structure of turbulence at high shear rate. *J. Fluid Mech.* **216**, 561–583.

Lumley, J. L. 1964 Spectral energy budget in wall turbulence. *Phys. Fluids* **7** (2), 190–196.

Lumley, J. L. & Panofsky, H. A. 1964 *The Structure of Atmospheric Turbulence*. Interscience Publishers.

Maxey, M. R. 1982 Distortion of turbulence in flows with parallel streamlines. *J. Fluid Mech.* **124**, 261–282.

Moffat, H. K. 1967 The interaction of turbulence with strong wind shear. In *Proceedings of the International Colloquium on Atmospheric Turbulence and Radio Wave Propagation* (ed. A. M. Yaglom & V. I. Tatarsky), Nauka, Moscow, pp. 139–156.

Mydlarski, L. & Warhaft, Z. 1996 On the onset of high-Reynolds-number grid-generated wind tunnel turbulence. *J. Fluid Mech.* **320**, 331–368.

Pope, S. B. 2000 *Turbulent Flows*. Cambridge University Press.

Press, W. H., Teukolsky, S. A., Vetterling, W. T. & Flannery, B. P. 1999 *Numerical Recipies in Fortran*. Cambridge University Press.

Rogallo, R. S. 1981 Numerical experiments in homogeneous turbulence. *Tech. Rep.* 81315. NASA.

Rogers, M. M. 1991 The structure of passive scalar field with uniform mean gradient in rapidly sheared homogeneous turbulent flow. *Phys. Fluids* A **3**(1), 144–154.

Rogers, M. M., Moin, P. & Reynolds, W. C. 1986 The structure and modelling of the hydrodynamics and passive scalar fields in homogeneous turbulent shear flow. *Tech. Rep.* TF-25. NASA Ames Centre for Turbulence Research.

Rohr, J. J., Itsweire, E. C., Helland, K. N. & van Atta, C. W. 1988 An investigation of the growth of turbulence in a uniform-mean-shear flow. *J. Fluid Mech.* **187**, 1–33.

Rose, W. G. 1966 Results of an attempt to generate a homogeneous turbulent shear flow. *J. Fluid Mech.* **25**, 97–120.

Rose, W. G. 1970 Interaction of grid turbulence with a uniform mean shear. *J. Fluid Mech.* **44**, 767–779.

Rotta, J. 1951 Statistische theorie nichthomogener turbulenz 1. *Z. Phys.* **129**, 547–572.

Savill, A. M. 1987 Recent developments in rapid-distortion theory. *Annu. Rev. Fluid Mech.* **19**, 531–573.

Schumacher, J. 2004 Relation between shear parameter and Reynolds number in statistically stationary turbulent shear flows. *Phys. Fluids* **16**, 3094–3102.

Schumacher, J., Sreenivasan, K. R. & Yeung, P.-K. 2003 Derivative moments in turbulent shear flow. *Phys. Fluids* **15**, 84–90.

Shen, X. & Warhaft, Z. 2000 The anisotropy of small scale structure in high Reynolds number (R_λ) turbulent shear flow. *Phys. Fluids* **12**, 2942.

Shih, L. H., Koseff, J. R., Ferziger, J. H. & Rehmann, C. R. (2000). Scaling and parameterization of stratified homogeneous turbulent shear flow. *J. Fluid Mech.* **412**, 1–20.

Tavoularis, S. 1985 Asymptotic laws for transversely homogeneous turbulent shear flows. *Phys. Fluids* **28** (3), 999–1001.

Tavoularis, S., Bennett, J. C. & Corrsin, S. 1978 Velocity-derivative skewness in small Reynolds number, nearly isotropic turbulence. *J. Fluid Mech.* **88**, 63–69.

Tavoularis, S. & Corrsin, S. 1981 Experiments in nearly homogeneous turbulent shear flow with a uniform mean temperature gradient. Part 1. *J. Fluid Mech.* **104**, 311–347.

Tavoularis, S. & Karnik, U. 1989 Further experiments on the evolution of turbulent stresses and scales in uniformly sheared turbulence. *J. Fluid Mech.* **204**, 457–478.

Thacker, W. D., Grosh, C. E. & Gatski, T. B. 1999 Modelling the dynamics of ensemble-averaged linear disturbances in homogeneous shear flow. *Flow Turbul. Combust.* **63**, 39–58.

Townsend, A. A. 1970 Entrainment and the structure of turbulent flow. *J. Fluid Mech.* **14**, 13.

Townsend, A. A. 1976 *The Structure of Turbulent Shear Flow*. Cambridge University Press.

Yu, D. & Girimaji, S. S. 2005 DNS of homogeneous shear turbulence revisited with the lattice Boltzmann method. *J. Turbul.* **6**, 1–17.